Response of a bubble bearing viscoelastic fluid to rapid decompression: Implications for explosive volcanic eruptions

Atsuko Namiki[a,b,*], Michael Manga[a]

[a]University of California, Berkeley, Department of Earth and Planetary Science, 307 McCone Hall, Berkeley, CA 94720-4767, U.S.A.
[b]Department of Earth Science, Kanazawa University, Kakuma, Kanazawa, Ishikawa 920-1192, Japan

Abstract

We conducted rapid decompression experiments using bubble-bearing viscoelastic fluid in a vertical shock tube. We varied vesicularity ϕ and pressure difference between the inside P_g and the outside P_o of the bubbles, $\Delta P = P_g - P_o$, to understand the behavior of bubbly-magmas under rapid decompression. We find that the potential energy, which depends on the initial vesicularity ϕ, P_g, and P_o, determines the expansion velocity of the bubbly fluid during rapid decompression. Higher potential energy, caused by a higher ϕ and a larger ΔP, leads to faster expansion. The expansion style also depends on the vesicularity ϕ and on the pressures P_g and P_o. We observe five different styles of expansion during the rapid decompression that depend on ϕ and ΔP. When both ϕ and ΔP are small, "nothing" occurs. As ϕ and ΔP increase, the bubbly fluid reacts more violently. First, the surface of the bubbly fluid "deforms" and the fluid elongates in the vertical direction. For sufficient elongation the fluid can "detach" from the tube wall. As ϕ and ΔP continue to increase, bubble walls can break, a process we refer to as "partial rupture". Finally, for still larger ΔP and ϕ, both bubble walls and plateau borders break allowing the fluid to "fragment" into discrete pieces and erupt explosively. Our experiments show that a larger potential energy, which results from higher ϕ and larger ΔP, causes a faster expansion of magma which in turn promotes fragmentation and thus explosive eruption. If we assume that the pressure inside bubbles P_g scales with the depth of bubbly magma, measuring the magma vesicularity in conduits or domes as a function of the depth before eruption would help assess volcanic hazard.
© 2005 Elsevier B.V. All rights reserved.

Keywords: explosive eruption; fragmentation; vesicularity

* Corresponding author. University of California, Berkeley, Department of Earth and Planetary Science, 307 McCone Hall, Berkeley, CA 94720-4767, U.S.A. Tel.: +1 510 642 6331; fax: +1 510 643 9980.
E-mail addresses: namiki@eps.berkeley.edu (A. Namiki), manga@seismo.berkeley.edu (M. Manga).
URL: http://www.seismo.berkeley.edu/namiki/ (A. Namiki).

1. Introduction

The 1980 explosive eruption of Mount St. Helens followed a large landslide, which caused rapid decompression of subsurface magma [1]. This event indicates that rapid decompression of magma may be

important for initiating explosive eruptions. Because a rapid decompression can fragment continuous magmas into discrete pieces [2], the eruption following decompression may ultimately become explosive [3–5].

Three basic models have been proposed for the mechanism of fragmentation. First, in the "critical vesicularity model", a critical vesicularity determines the fragmentation threshold [3]. Second, in the "brittle failure model", the liquid magma behaves similar to solid magma, and the bubble walls fail when the maximum stress exceeds the strength of the magma. This theory has been applied to molten magma to predict the fragmentation threshold [6–8]. Third, the "relaxation time scale model" is based on the idea that when strain rates during deformation exceed the inverse relaxation time of melt, $1/t_r$, brittle fragmentation may result [9–12].

Preexisting bubbles should be important for magmas to react explosively to a rapid decompression. The stress distribution around bubbles strongly depends on the vesicularity [8]: larger vesicularity can generate a larger tensile stress under the same overpressure. Deformation of the magma by rapid decompression also should depend on the vesicularity. Because the gas inside the bubbles is much more compressible than the surrounding magma, the volume change caused by decompression will be dominated by bubble expansion [13–16]. Laboratory experiments confirm that preexisting bubbles reduce the overpressure required for fragmentation [17–20]. In addition, the texture of pumice is often consistent with eruption of a bubbly magma that experiences rapid decompression [21].

The response of bubbly fluid to rapid decompression is not yet understood, despite its importance. Because this problem involves several interacting physical processes and properties, including viscoelasticity, fragmentation, shock wave propagation, and two-phase flow, it is a challenging problem to study using theoretical and numerical approaches. We thus use an experimental approach with analogue fluids [22], in which we can control the fluid's vesicularity and viscoelastic properties. We focus on observing and characterizing the response of bubbly fluid to rapid decompression in order to study the effects of preexisting bubbles on eruptions induced by rapid decompression.

2. Experimental method

The decompression experiments are conducted in a shock tube type apparatus (Fig. 1). The bubbly fluid, our analogue magma, is contained in the shock tube and is separated from a large low-pressure tank by diaphragms. When the diaphragms break, a rarefaction wave propagates into the tube, and the bubbly fluid experiences rapid decompression. The shock tube is made of a polycarbonate and has an internal diameter of 50 mm and a length of 250 mm. The volume of the low-pressure tank is 0.18 m^3. The initial sample pressure P_g is 10^5 Pa, and pressure inside the low-pressure tank P_o is variable. Two diaphragms are inserted between the high-pressure tube and the low-pressure tank. Diaphragms disrupt because of the pressure differential across it. We use four kinds of diaphragms to change the initial pressure difference; 2, 4.8, 6 μm thickness polyethylene films and commercial aluminum foil. When the diaphragms rupture, the disruption of the film or foil is nearly complete, resulting in an opening that is essentially the same size as the outlet to the shock tube. We can control the timing of diaphragm rupture and adjust the pressure difference between two tanks by changing the pressure inside the small space between the two dia-
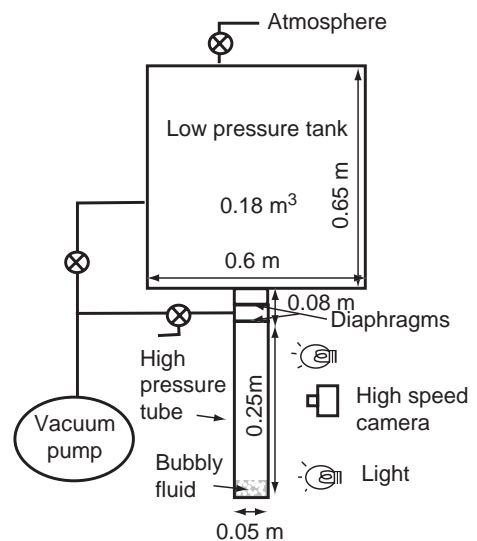

Fig. 1. Illustration of experimental apparatus. The dimension of the high pressure tube is 0.05 m in diameter, 0.25 m in length, and 4.9×10^{-4} m^{-3} in volume. The low pressure tank is 0.6 m in diameter, 0.65 m in length, and 0.18 m^{-3} in volume.

phragms. Images of the reaction of the bubbly fluid are recorded by a high speed digital video camera at a rate of 2000 frames/s with resolution of 1280×256 pixels. To obtain a better image, two lights illuminate the high pressure tube. The heat produced by the lamps can increase the pressure and temperature inside the tube, but never to more than 1.03×10^5 Pa and 40 °C, respectively. Because the lights are placed at the top and bottom of the high pressure tube, the center of the tube appears darker than the top and bottom in some images.

For our magma analogue, we use xanthan gum solution, which is a viscoelastic fluid (Ina Food Industry Co.). We use three different concentrations of xanthan gum in water, 0.1, 0.3, and 0.5 wt.%, to characterize the viscosity dependence of the decompression dynamics. Xanthan gum solutions shows strong shear-rate dependence of viscosity, and a higher concentration provides a larger viscosity as shown in Fig. 2. Fig. 3 shows the measured storage G' and loss G'' moduli of xanthan gum solutions. When the storage modulus is much lower than the loss modulus, i.e., $G' \ll G''$, the fluid behaves as a "liquid-like" fluid. On the other hand, when $G' \gg G''$, and G' is nearly frequency-independent, the fluid is "solid-like". The frequency at the crossover of G' and G'' is the characteristic relaxation time. Thus, when the xanthan gum concentration is 0.1 wt.%, the relaxation time is around 1 s

Fig. 3. The measured storage G' and loss G'' moduli of xanthan gum solution with no bubbles. Larger symbols and solid lines show the storage modulus, and smaller symbols and dotted lines show the loss modulus. Crosses, circles, and asterisks show the concentration of xanthan gum which are 0.1, 0.3, and 0.5 wt.%, respectively.

and when xanthan gum concentration is higher than 0.3 wt.%, the relaxation time is longer than 10 s. Viscosity and dynamic moduli are measured with a cone-and-plate rheometer (Thermo Haake Rheoscope).

Bubbles are added to the fluid by a hand mixer. Vesicularity is controlled by the duration of beating. The average bubble radii are 0.13, 0.080, and 0.063 mm for 0.1, 0.3, and 0.5 wt.% solutions, respectively. These are measured with a microscope within 30 min after beating. Bubble radii increase in time through coalescence. Experiments are performed within 30 min after beating except for experiment a′ in Table 1. The distribution of bubble radii is exponential or unimodal rather than power law. To decrease surface tension, 0.4 vol.% of surfactant (Walgreens hand soap) was added to the xanthan gum solutions. Estimated surface tension is between 73 and 35 mN m^{-1} which is a typical value for fresh water and water saturated with surfactant, respectively [23]. Measured viscosity and dynamic moduli with and without surfactant are the same. Vesicularity is calculated by measuring the weight and volume of the beaten fluid. The bubbly fluid is poured into the high pressure tube from the top. When we pour even bubble-free fluid, a small number of bubbles are created and entrained into the fluid. From photographs we estimate a vesicularity of about 0.01, and thus assume this is the lowest vesicularity in our experiments. In experiments with bubbly fluids, we expect a similar
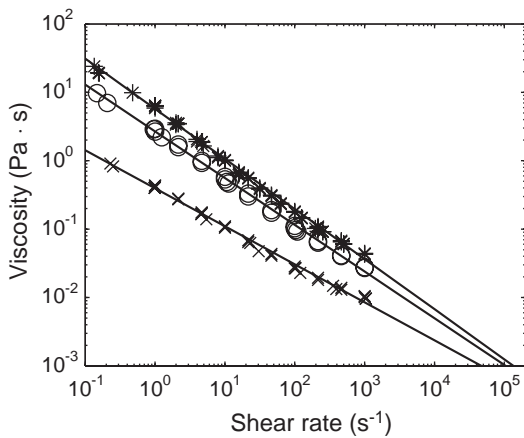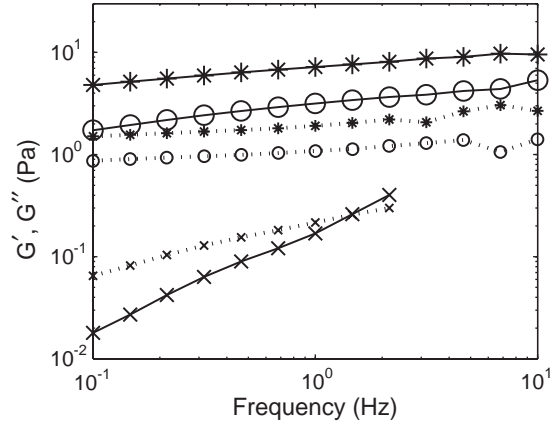

Fig. 2. The viscosity of xanthan gum solution as a function of shear rate. Crosses, circles, and asterisks show the concentration of xanthan gum in water which are 0.1, 0.3, and 0.5 wt.%, respectively, and each line is calculated by $\eta = 0.40\dot{\gamma}^{-0.55}$, $\eta = 2.7\dot{\gamma}^{-0.68}$, $\eta = 5.7\dot{\gamma}^{-0.73}$, respectively.

Table 1
Experimental conditions and results

ϕ	$P_g \times 10^5$ (Pa)	$P_o \times 10^5$ (Pa)	$\Delta P \times 10^5$ (Pa)	Concentration (wt.%)	v_e (m s^{-1})	Pattern	
$O(10^{-2})$	1.00	0.35	0.65	0.1	0.00	Nothing	
0.53	1.01	0.37	0.64	0.1	8.70	Fragmentation	a′
0.66	1.00	0.10	0.90	0.1	15.20	Fragmentation	
0.66	0.99	0.77	0.22	0.1	2.60	Detachment	
0.65	1.01	0.34	0.67	0.1	11.60	Fragmentation	
$O(10^{-2})$	1.01	0.48	0.53	0.3	0.00	Nothing	
0.18	0.99	0.20	0.79	0.3	3.90	Detachment	
0.41	1.02	0.14	0.88	0.3	14.80	Fragmentation	
$O(10^{-2})$	1.03	0.34	0.69	0.5	0.00	Nothing	e
0.08	1.00	0.09	0.91	0.5	6.40	Partial rupture	
0.10	1.00	0.07	0.93	0.5	7.30	Detachment	
0.13	1.00	0.35	0.65	0.5	3.30	Detachment	
0.13	0.99	0.79	0.20	0.5	0.80	Nothing	
0.15	0.99	0.36	0.63	0.5	4.20	Detachment	
0.22	1.01	0.07	0.94	0.5	12.60	Fragmentation	
0.23	1.01	0.35	0.66	0.5	3.90	Detachment	c
0.26	1.01	0.41	0.60	0.5	4.80	Detachment	
0.27	1.01	0.25	0.76	0.5	10.47	Partial rupture	
0.34	1.01	0.08	0.93	0.5	13.60	Fragmentation	
0.41	1.00	0.80	0.20	0.5	1.80	Deformation	
0.46	1.02	0.43	0.59	0.5	7.58	Partial rupture	
0.48	1.00	0.44	0.56	0.5	8.40	Detachment	
0.58	1.00	0.79	0.21	0.5	2.60	Deformation	d
0.58	1.01	0.06	0.95	0.5	18.10	Fragmentation	a
0.60	1.00	0.11	0.89	0.5	21.77	Fragmentation	
0.63	1.00	0.48	0.52	0.5	10.75	Partial rupture	
0.63	1.02	0.15	0.87	0.5	18.00	Fragmentation	
0.63	1.00	0.04	0.96	0.5	26.45	Fragmentation	
0.65	1.01	0.40	0.61	0.5	15.13	Partial rupture	
0.69	0.90	0.24	0.66	0.5	18.36	Fragmentation	
0.71	1.03	0.09	0.94	0.5	33.79	Fragmentation	
0.78	1.00	0.40	0.60	0.5	13.40	Fragmentation	
0.79	1.00	0.59	0.41	0.5	8.30	Partial rupture	b

small change in vesicularity as the fluid is poured into the shock tube. The segregation of bubbles from the liquid within the shock tube is not observed except for experiment a′ (Table 1) and we thus assume that the bubbles are distributed uniformly in the liquid. The volume fraction of dissolved air in water under atmospheric pressure is less than 2 vol.%, is sufficiently small compared to the volume of mechanically added bubbles, and does not influence our conclusions. Experiments are conducted at higher pressure and lower temperature than the evaporation curve of water, so the expansion of preexisting bubbles, rather than boiling, should dominate the volume change.

We conduct a series of experiments with varying initial vesicularity ϕ, initial pressure difference bet-

ween two tanks (overpressure) $\Delta P = P_g - P_o$, and viscoelastic properties.

3. Results

Experiments show that larger initial vesicularity ϕ and larger overpressure ΔP generate faster expansion of bubbly fluids. The expansion patterns also depend on vesicularity and overpressure. Fig. 4 summarizes the experimental results. We observe five styles of expansion following rapid decompression: (a) fragmentation, (b) partial rupture, (c) detachment, (d) deformation, and (e) nothing. Only in the case of fragmentation (a) is the decompressed fluid
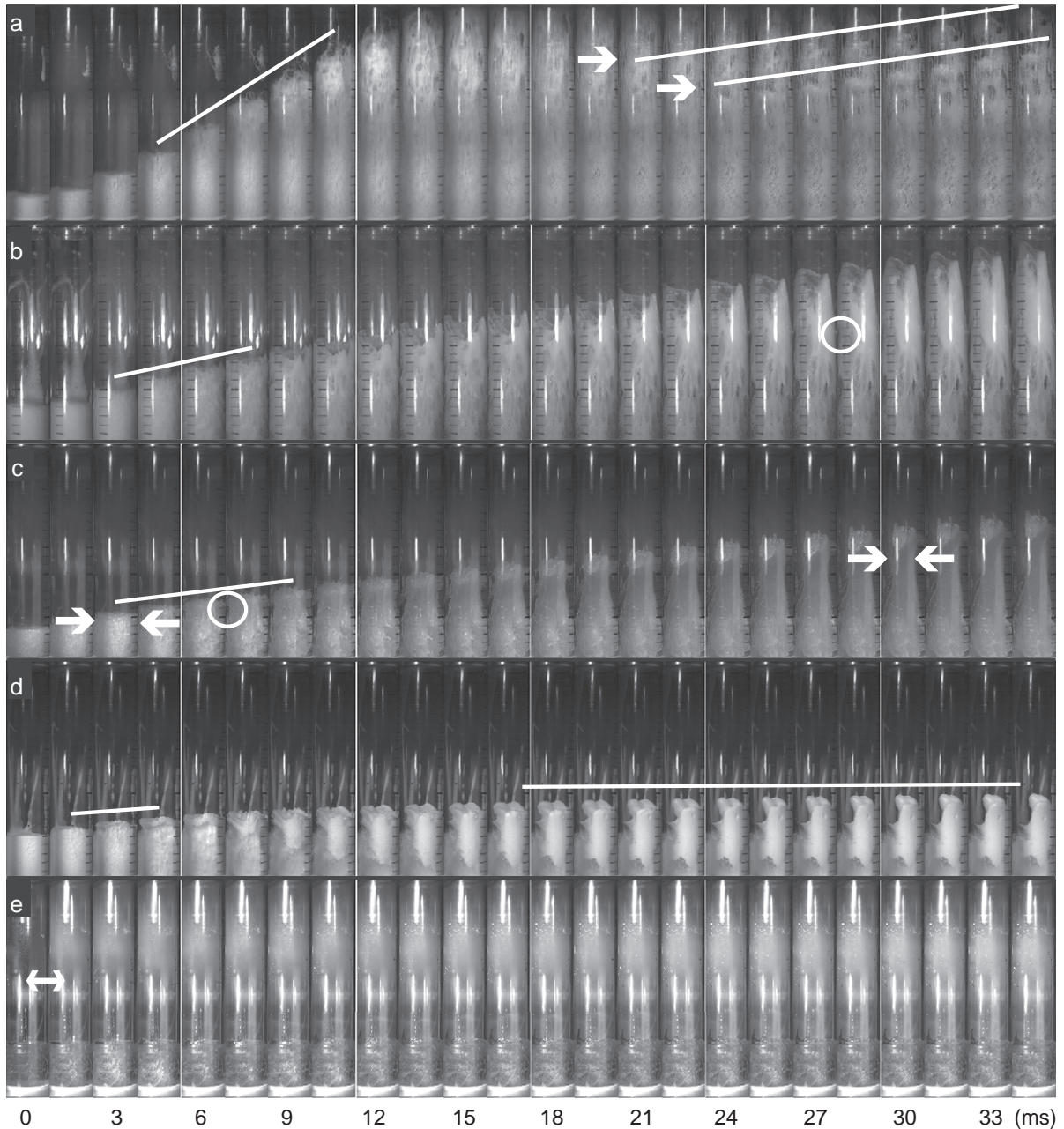
Fig. 4. Digital photographs showing the response of the bubbly fluid in the shock tube. The interval between images is 1.5 ms. The height is 0.25 m, and the diameter is 0.05 m. The brightness of the fluid depends on vesicularity. The five experiments show (a) fragmentation ($\phi=0.58$, $\Delta P=9.5\times10^4$ Pa), (b) partial rupture ($\phi=0.79$, $\Delta P=4.1\times10^4$ Pa), (c) detachment ($\phi=0.23$, $\Delta P=6.6\times10^4$ Pa), (d) deformation ($\phi=0.58$, $\Delta P=2.1\times10^4$ Pa), and (e) nothing ($\phi=O(10^{-2})$, $\Delta P=6.9\times10^4$ Pa).

ejected from the shock tube. Details of the experimental conditions and results are summarized in Table 1.

Fig. 4a shows a typical example of "fragmentation". The fluid expands rapidly as the bubbles expand (6 ms). As the bubbly fluid expands vertically,

larger bubbles form. These appear to be generated by breaking bubble walls and through bubble coalescence (12 ms). Finally, the fluid fragments layer by layer, which is observed as white and black bands, as indicated by arrows in the figure (24–34.5 ms). The bands migrate upward (24–34.5 ms). At the end of the experiment, only a small fraction of the fluid remains in the shock tube: most of the fluid is ejected into the low-pressure tank and hits the tank's roof.

Fig. 5a′1–4 shows enlarged photographs of case a′. We show this case instead of Fig. 4a, because the expansion velocity of Fig. 4a is too fast and preexisting bubbles are too small to see details. Case a′ is conducted after waiting an hour so that coalescence of preexisting bubbles produces larger radii. The dark
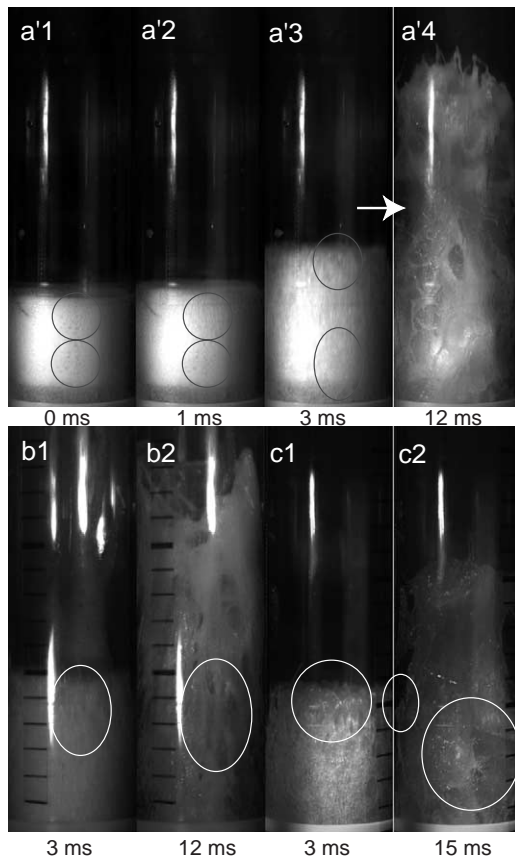

Fig. 5. Enlarged photographs. The height is 0.15 m, and the diameter is 0.05 m. (a′1–a′4) Snap shots for a case with $\phi = 0.53$, $\Delta P = 6.4 \times 10^4$ Pa, at 0, 1, 3, 12 ms. (b1, b2) Enlarged photographs of Fig. 4b at 3, 12 ms. (c1, c2) Enlarged photographs of Fig. 4c at 3, 15 ms.

region at the bottom of the tube is accumulated liquid. The vesicularity in the white region is larger than the measured value. At 1 ms, the rarefaction wave has propagated downward and reached the middle of the bubbly fluid; bubbles observed at 0 ms have disappeared and are replaced by vertical black streaks in the upper half of the bubbly fluid. This indicates that the decompression wave elongates bubbles which are observed as black streaks. In deeper parts of the shock tube, undeformed bubbles still exist. This suggests that the rarefaction wave deforms each bubble rather than the whole fluid at this stage of the decompression. At 3 ms, the black streaks reach at the bottom of the tube and also become wider. At 12 ms, much of the fluid in the middle of the tube appears to have been evacuated, suggesting that fragmentation has occurred.

Sometimes we observe structures which resemble those observed in the fragmentation cases, but do not observe the critical moment of fragmentation. These situations arise when fluids that adhere to the tube wall make the inside invisible, or when the images do not extend far enough up the shock tube. We thus classify experiments in which we directly observe discrete fragments or in which fluid ejected from the tube hits the roof of the low-pressure tank as fragmentation. In all cases, the maximum volume expansion of bubbly fluid without inertia is insufficient to cause the fluid to enter the low-pressure tank. Hence, fluid can only be ejected into the low pressure tank if it undergoes fragmentation. We refer to this style of expansion as 'explosive' expansion.

"Partial rupture" is shown in Fig. 4b. An enlarged photograph is shown in Fig. 5b1,2. The vesicularity is larger than that in Fig. 4a but the overpressure is smaller than that in Fig. 4a. When the rarefaction wave arrives, bubbles elongate parallel to the tube, as they do in Fig. 5a′ (Fig. 5b 3 ms). The fluid expands more slowly than in Fig. 4a, and a texture that resembles a net develops (Fig. 5b 12 ms). This structure then moves upward and the liquid phase accumulates at the top of the expanding fluid (18 ms). As the fluid stretches, it detaches from the tube wall, which is indicated by a circle in Fig. 4b (27 ms). In this case, both the liquid and gas become continuous phases, whereas in the process depicted in Fig. 4a, fragmentation-disrupted fluid forms discrete

parcels. In Fig. 4b, gas can escape from the bubbly liquid.

"Detachment" is shown in Fig. 4c. An enlarged photograph is shown in Fig. 5c1,2. Both vesicularity and overpressure are smaller than those in Fig. 4a. When the rarefaction wave arrives, bubbles and the entire fluid column are stretched vertically (3 ms). Subsequently, the fluid detaches from the tube wall (6 ms), indicated by a circle in the figure. The detached fluid has a mesh pattern, as shown in Fig. 5c (15 ms), and stretches without interacting with the walls. Because of its detachment, the horizontal width of the fluid column decreases, as indicated by arrows at 3 and 30 ms in the figure.

"Deformation" is shown in Fig. 4d. The vesicularity is almost the same as that in Fig. 4a but the overpressure is smaller than that in Fig. 4b. When the rarefaction wave arrives, the bubbles elongate vertically. Some bubbles interconnect, and the top of the fluid rises upward (6 ms). However, the final height caused by expansion is much smaller than that observed in previous cases, as denoted by a white line in the figure.

Fig. 4e shows the case in which "nothing" occurs. The change of the background color between the first and second images shows the arrival of the rarefaction wave because the mist formed by decompression reflects the light used to illuminate the fluid. After the arrival of the rarefaction wave preexisting bubbles gradually expand until 4.5 ms; this is observed as an increase in reflection intensity. Small white spots are generated in the fluid where the color was initially observed as black. The resolution of the images, however, is not sufficient to determine whether the black region indicates that the initial bubbles are too small to be observed or that there are no bubbles in which case the white spots represent nucleated bubbles. After the expansion of bubbles, the bubbles and surface of the fluid oscillate in the vertical direction. The reflection intensity (amount of bubbles) decreases after 6 ms, suggesting the escape or dissolution of bubbles. The mist and the fluid surface oscillate at the same frequency. Upward and downward motion of the fluid surface increases and decreases the reflection intensity, respectively, implying the expansion and shrinkage of bubbles, respectively. The volume change of the bubbly fluid, however, is negligible.

4. Discussion

4.1. Expansion velocity

Larger pressure changes and vesicularity cause faster expansion, as shown by the white lines in Fig. 4. The expansion can be divided into three stages: acceleration, constant velocity, and deceleration, though in some cases only one or two stages are actually recorded. The position of the flow front, as a function of time, in the three stages can be described by polynomials of degree 2, degree 1, and degree 2, respectively. We refer to the slope of the second regime as the "expansion velocity". Here, we determine the expansion velocity using at least three data points that maximize the velocity. Table 1 lists the

Table 2
Notations

ϕ	Initial vesicularity	
P_g	Initial pressure inside of bubbles	Pa
P_o	Pressure outside of bubbles	Pa
ΔP	$P_g - P_o$	Pa
t_r	Relaxation time scale	s
G'	Storage modulus	Pa
G''	Loss modulus	Pa
$\dot{\gamma}$	Shear rate	s^{-1}
v_e	Expansion velocity of bubbly fluid	$m\ s^{-1}$
$\Delta\hat{H}_{mod}$	Potential energy defined by Eq. (A.7)	$J\ m^{-3}$
γ	Isentropic exponent	
ρ_f	Density of the bubbly liquid	$kg\ m^{-3}$
E	Young's modulus	Pa
σ	Poisson's ratio	
ϵ	Axial strain (cylindrical coordinates)	
ϵ_c	Critical axial strain to break	
σ^{rr}	Radial stress	Pa
u_{rr}	Radial strain	
$u_{\theta\theta}$	Tangential strain	
$u_{\theta\theta c}$	Critical tangential strain to break	
r	r component of vector in spherical coordinate system	
R_1	Bubble radius	m
R_2	Outer radius of bubble shell	m
ρ_g	Density of the gas phase	$kg\ m^{-3}$
H_0	Volumetric reservoir enthalpy	$J\ m^{-3}$
$\Delta\hat{H}$	Volumetric enthalpy change	$J\ m^{-3}$
$\Delta\hat{W}$	Volumetric work done to the low pressure chamber	$J\ m^{-3}$
$d\hat{V}$	Volumetric volume change	
$\Delta\hat{U}$	Volumetric change of internal energy	$J\ m^{-3}$
$\Delta\hat{Q}$	Volumetric additional heat	$J\ m^{-3}$
$O(x)$	x order of magnitude	

measured expansion velocity. Next we calculate the expansion velocity theoretically.

Assuming that the gas inside the bubble expands adiabatically, and that the change of the volumetric enthalpy caused by a decompression, $\Delta\hat{H}_{mod}$, is transformed to kinetic energy, the expansion velocity v_e can be written as (see Appendix A).

$$\Delta\hat{H}_{mod} = \phi \cdot \frac{\gamma P_g - P_o}{\gamma - 1}\left[1 - \frac{\gamma P_o}{\gamma P_g - P_o}\right.$$
$$\left. \times\left\{\left(2 - \frac{1}{\gamma}\right)\left(\frac{P_g}{P_o}\right)^{1/\gamma} - 1\right\}\right] \quad (1)$$

$$v_e = \left(\frac{2\Delta\hat{H}_{mod}}{\rho_f}\right)^{1/2}, \quad (2)$$

where $\gamma = 1.4$ is the isentropic exponent, P_o is the outside pressure, P_g is the gas pressure inside of bubbles, and ρ_f is the density of the bubbly fluid (see Table 2). Here, $\Delta\hat{H}_{mod}$ is determined by P_g, P_o, and ϕ, so that the expansion velocity is determined solely by P_g, P_o, and ϕ. When $P_g \gg P_o$, $\Delta\hat{H}_{mod} \sim \phi\gamma P_g/(\gamma - 1)$. This formulation and these assumptions are similar to those previously used to estimate pyroclastic flow velocities [24] and steamblast eruptions
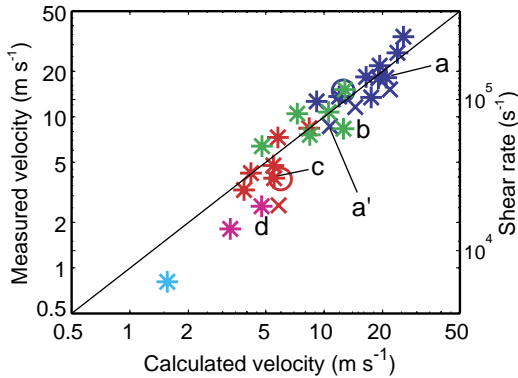

Fig. 6. Correlation between measured and calculated expansion velocities. Blue, green, red, pink, and light-blue symbols show cases with fragmentation, partial rupture, detachment, deformation, and "nothing," respectively. Attached numbers a–d, and a' correspond to experiments shown in Figs. 4 and 5. Crosses, circles, and asterisks indicate concentrations of xanthan gum solutions of 0.1, 0.3, and 0.5 wt.%, respectively. Vertical axis on the right shows the calculated shear rate v_e/R_1, where $R_1 \sim 0.13$ mm is the averaged bubble radius for a concentration of 0.1 wt.%. Radius for 0.1 wt.% is the largest value for the three different solutions, so this shear rate represents a minimum estimate.

[25]. Fig. 6 shows a good correlation between measured and calculated velocities.

Fig. 6 also indicates that the expansion velocity does not depend on viscosity, because this figure includes three different fluids whose viscosities vary more than one order of magnitude at the same shear rate. If the shear rate caused by expansion exceeds the inverse relaxation time of the bubbly fluid, $1/t_r$, the fluid behaves as an elastic material, and the expansion velocity is determined by the potential energy. Indeed, in our experiments the shear rate calculated from the measured expansion velocity is faster than $1/t_r \sim 1$ s^{-1}. The vertical axis on the right-hand side of Fig. 6 is the calculated shear rate v_e/R_1, where $R_1 \sim 0.13$ mm is the averaged bubble radius. We thus conclude that the fluids behave as elastic materials over the time scales that bubbles expand and films rupture (Figs. 4 and 5) so that $\Delta\hat{H}_{mod}$ determines the expansion velocity. Because $\Delta\hat{H}_{mod}$ determines the expansion velocity, we refer to this quantity as potential energy.

4.2. Response patterns

Fig. 7 is the regime diagram for the response of our bubbly fluids. Next we explain the physical processes that result in the five distinct expansion styles. Fig. 8a illustrates schematically the processes we describe.

When the rarefaction wave arrives at the first line of bubbles, a pressure difference is generated between bubbles and the atmosphere. This deforms bubble walls and the potential energy $\Delta\hat{H}_{mod}$ is transformed to kinetic energy, $\rho_f v_e^2/2$. Because the fluid is initially confined by the tube, the bubbly fluid has a velocity only in the vertical direction. Thus, the column of the bubbly fluid is stretched vertically. The shape reflects the Poisson's ratio, and the fluid can potentially "detach" from the tube wall as observed in Fig. 4c. The kinetic energy, $\rho_f v_e^2/2$, is used to deform each bubble and hence to stretch the whole fluid, and is stored as elastic energy.

If the bubble walls rupture, however, the bubble walls release elastic energy and expand radially. Thus, the bubbly fluid can expand both in the vertical and radial directions and does not detach from the tube wall. If only thin films around bubbles rupture but the thick plateau borders that exist at the points of contact between three or more bubbles remain, the texture resembles a net. In addition, film rupture
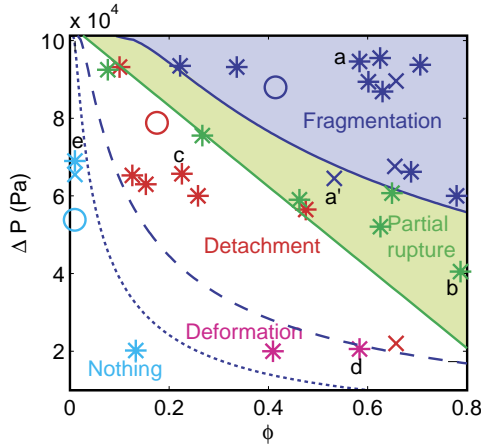
Fig. 7. Regime diagram for the response of bubbly fluid as a function of initial vesicularity ϕ and overpressure ΔP. Symbols are the same as those in Fig. 6. Solid, dashed and dotted blue lines show $\Delta \hat{H}_{mod}$=30 k, 5 k, and 2 kJ m^{-3}, respectively. Green line is calculated by Eq. (3) where Poisson's ratio is assumed as σ=0.5. Blue and green regions indicate fragmentation and partial rupture, respectively.

leads to thickening of the plateau borders [26] and thus enhances the net texture. We suggest that "partial rupture" observed in Fig. 4b is the result of this process.

The threshold for partial rupture can be calculated by assuming that, bubble walls break when the strain exceeds a critical value. The tangential component of the strain tensor, $u_{\theta\theta}$, of a bubble wall is given by Eq. (B.2) (Appendix B). Here $u_{\theta\theta}$ has a minimum at $r=R_1$, so that if $u_{\theta\theta}(r=R_1)$ exceeds a critical strain $u_{\theta\theta c}$, the bubble wall can break at any radius. This criterion is written as

$$\frac{-(P_o - P_g)}{E(1-\phi)}\left\{(1-2\sigma)+\frac{1+\sigma}{2}\right\}>u_{\theta\theta c}. \qquad (3)$$

This threshold is denoted in Fig. 7 by the green line where σ=0.5 and $Eu_{\theta\theta c}$=78 k Pa, and does appear to separate partial rupture from detachment. Small differences from the prediction may be attributed to the variation of bubble radii.

After the bubble walls break and the texture resembling a net expands, the liquid's elasticity reduces the expansion velocity. Because the kinetic energy of the fluid causes the fluid to deform, and velocity decreases with height in the column of fluid, the

relaxation of elastic stresses draws fluid to the top of the fluid column, as observed in Fig. 4b. The elasticity also acts to detach fluid from the tube wall.

If the axial strain of the plateau borders ϵ exceeds a critical value after the bubble walls break, the plateau borders can also fragment. The texture termed "fragmentation" in Fig. 4a is the result of this process. The maximum elastic energy for the plateau borders should reflect the initial potential energy $\Delta \hat{H}_{mod}$. The criteria for the fragmentation of a plateau border can thus be written as

$$\Delta \hat{H}_{mod}>E\epsilon_c^2 \qquad (4)$$

where E is Young's modulus and ϵ_c is the critical axial strain for the fragmentation. The solid blue line in Fig. 7 shows a constant potential energy, $\Delta \hat{H}_{mod}$= 30 k J m^{-3}, and separates fragmentation from partial rupture.

In the case of detachment, fragmentation of the stretched bubbly fluid is not observed—in contrast to the scenario shown in Fig. 8. However, fragmentation as illustrated in Fig. 8 might still be possible if the fluid has another driving force for expansion. Lane et al. [27] shows fragmentation with detachment where bubbles grow by the exsolution of organic solvent (volatile) in gum rosin. In their case, the driving force of the expansion is exsolution of the volatile component because the fluid should almost be bubble-free prior to expansion. Instead of initially existing bubbles, exsolution and nucleation create new bubbles. In this case, the pressure difference between the inside and outside of bubbles should be small so that each bubble would not experience sufficient strain to break. The stretched fluid could thus fragment without bubble-wall breakage.

Deformation and "nothing" are observed for smaller vesicularity and smaller overpressure. Dashed and dotted lines in Fig. 7 show constant potential energies of $\Delta \hat{H}_{mod}$=5 k and 2 k J m^{-3}, and are assumed to be representative of reasonable thresholds. The agreement with observations suggests that the threshold for deformation and "nothing" is also described by a constant potential energy. To detach the fluid from the tube wall, a finite potential energy may be required. To deform the surface of the fluid, another finite potential energy may be required. When the fluid fails to detach from the tube wall, viscous drag decele-
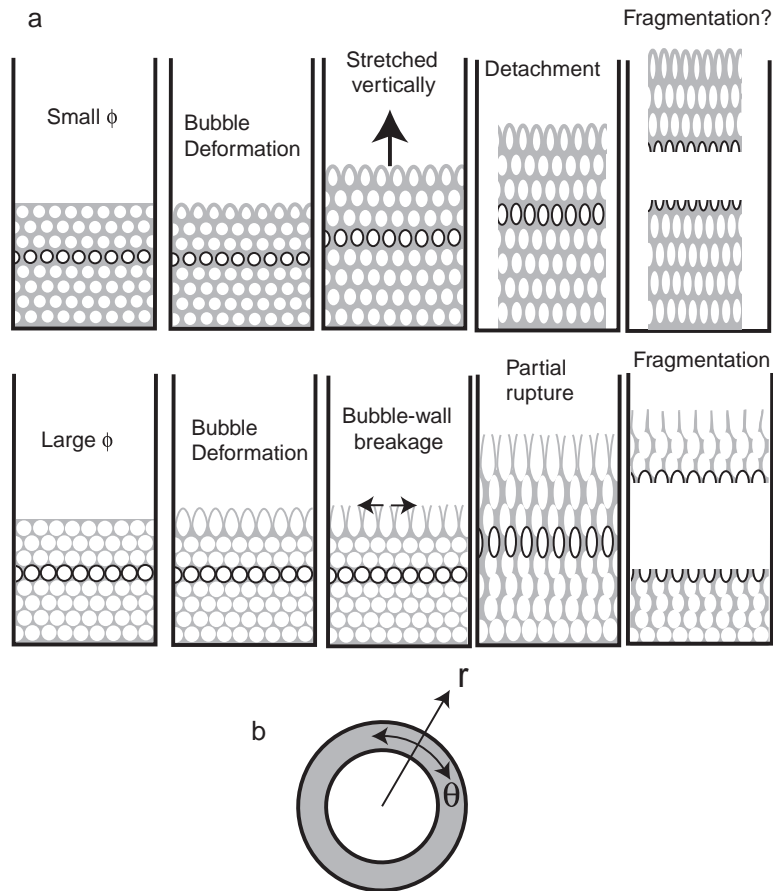
Fig. 8. (a) Schematic illustration of an expanding bubbly fluid. (b) Definition of spherical polar coordinates.

rates the fluid. Indeed, the measured expansion velocity for the deformation and "nothing" are lower than predicted from Eq. (2) as shown in Fig. 6.

We thus conclude that the style of expansion depends on the parts of the fluids that break or fragment. To break a bubbly fluid into many discrete pieces, both bubble walls and plateau borders should fragment. The thresholds for these two processes, at least in our experiments, are governed by the strain energy.

5. Implications for a volcanic eruption

We now apply our results to volcanic eruptions. First, we need to determine whether shear rates v_e/R_1 exceed the inverse relaxation time $1/t_r$ in volcanic eruptions: if $v_e/R_1 > O(1/t_r)$, magma will behave as an elastic material, and we can calculate the eruption velocity using Eq. (2). The relaxation times of natural magmas depend on composition and temperature, and for rhyolite at 800 °C, $t_r = O(10^1)$ s [9]. For the shear rate to exceed $v_e/R_1 > 10^{-1}$ s^{-1}, a combination of $R_1 < 0.01$ m and $v_e > 10^{-3}$ m s^{-1} is sufficient. A bubble radius of 0.01 m is quite large [28], and the expansion velocity can exceed 10^{-3} m s^{-1} with slight overpressure even at very low vesicularity (Fig. 9). Thus, when rapid decompression occurs and bubbles are present in the magma, the magma should respond as an elastic material, and we can calculate the expansion velocity by Eq. (2).

Next, we need to discuss whether the fragmentation thresholds determined in our experiments are relevant for magma fragmentation. Spieler et al. [20] have

found that the critical pressure for fragmentation is $P_g = 0.995/\phi$ MPa for a wide range of magmas at 850 °C. This means that a constant potential energy, which is a product of $P_g\phi$, determines the fragmentation threshold. The calculated critical potential energy for the magma fragmentation is 2.5 MJ m^{-3}, and this can deform a magma with $E = O(10^9)$ Pa to strains $\varepsilon = O(10^{-2}-10^{-1})$. Thus, the magma fragmentation threshold is consistent with our experimental results, and we hereafter assume we can apply our results to volcanic eruptions.

We adopt the results of Spieler et al. [20] for the fragmentation threshold and show the threshold in Fig. 9. Magmas with $\phi > 0.2$ can fragment at $P_g > 5$ MPa, and the eruption velocity should be greater than 50 m s^{-1} as seen in Fig. 9. This is similar to the maximum blast velocity observed during the 1980 eruption of Mount St. Helens [29].

The threshold for breaking bubble walls in experiments is well-described by Eq. (3). For magmas we do not know the critical strain for breaking bubble walls, $u_{\theta\theta c}$, so we cannot estimate the region for partial rupture.

In the region below the gray area in Fig. 9, detachment might occur. Unfortunately, for several reasons we do not have sufficient information to estimate the expansion patterns and thresholds bet-

ween "detachment", "deformation", and "nothing". First, because the shape of the deformed magma reflects the Poisson's ratio, it is not clear whether the detachment would occur in real magma. Second, volcanic conduits are deformable, unlike our shock tube, so that conduits may contract in response to the radial deformation of magma. Finally, the region of parameter space separating "deformation" from detachment may be quite small, and the range of parameters over which detachment will occur could also be quite narrow.

Here, we have not taken into account the effects of bubble nucleation and diffusive growth of bubbles during rapid decompression to explain the expansion velocity and style. We anticipate both effects to be of secondary importance for determining the initial expansion velocity and style during rapid decompression when the magma has a sufficiently high initial vesicularity for three reasons. First, because the radii of the newly nucleated bubbles are small [28], the contribution to the vesicularity which causes rapid bubble expansion is limited. Second, diffusive growth of the newly nucleated bubbles is slower than the expansion of the preexisting bubbles owing to the slow diffusion in high-viscosity magmas [13,15, 16,30]. Finally, the pressure difference between the inside and outside of newly nucleated bubbles, which provides the driving force of breaking bubble walls, will be smaller than that of preexisting bubbles. On the other hand, the expansion of preexisting bubbles ends immediately after decompression, but actual explosive volcanic eruptions can continue for many hours. Slow diffusive growth of newly nucleated bubbles is probably very important for sustained eruptions.

At active volcanoes, rapid decompression can occur following the sudden removal of a dome (plug) on the vent. If the plug is removed after the magma has sufficient vesicularity and overpressure, the magma may have a large enough initial potential energy for rapid expansion. If the potential energy exceeds the critical value for fragmentation, the magma fragments. Rapid expansion of gas released from broken bubbles will eject magmatic debris at high rates — the eruption style becomes explosive.

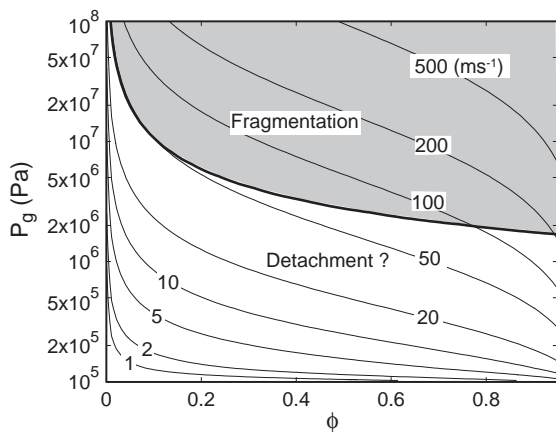However, if the plug is removed when the magma has lower vesicularity and overpressure,

Fig. 9. Bold, solid curve shows the fragmentation threshold for a critical potential energy of 2.5 MJ m^{-3}. Thin lines show calculated expansion velocity for magma as a function of P_g and vesicularity ϕ using Eq. (2). We assume that the density of bubble-free magma is 2200 kg m^{-3}, P_o is atmospheric pressure 10^5 Pa, and $\gamma = 1.4$.

the potential energy does not exceed the fragmentation threshold and the eruption will not become explosive. As shown in Fig. 5b, decompression can elongate bubbles and form textures similar to those found in real magma clasts with high-permeability [31,32]. If this type of decompression occurs repeatedly, the magma may be able to lose volatiles (degas) to the surrounding rock or atmosphere. It may then erupt effusively to form a lava dome with high permeability pumice. The permeability of magma has been considered to be an important factor in determining the eruption style [32–35]. Our experiments, for example the one shown in Fig. 5b, illustrate how bubble connections may develop as a result of decompression.

Our experiments and scaling indicate that the potential energy, which depends on ϕ, P_g, and P_o before rapid decompression, will determine the eruption velocity and style that follows rapid decompression. When P_g represents lithostatic pressure, the potential energy is dominated by vesicularity. If the depth distribution of magma vesicularity before eruption can be estimated by seismological methods or other remote observations, the hazard posed by magma bodies can be inferred.

Acknowledgments

Appendix A. Comparison of models of the expansion velocity

Several scaling laws have been proposed to explain the expansion velocity. In this Appendix, we compare these models with the experimental results.

Fink and Kieffer [24] and Mastin [25] estimated the blast velocity assuming isentropic expansion of the compressed gas,

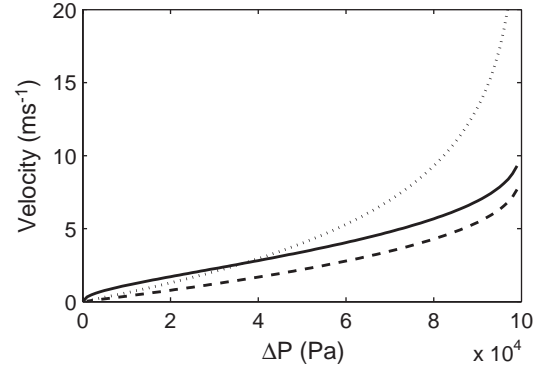$$v_e = \sqrt{2\hat{H}_o / \rho_g}, \tag{A.1}$$

Fig. A.1. Pressure dependence of the expansion velocities in three models. Solid, broken, and dotted lines show models H, U, and CT calculated by Eqs. (A.6), (A.10), (A.11), respectively. Here we assume density of the liquid phase is 1000 kg m^{-3}, $\phi = 0.25$, and $P_g = 10^5$ Pa, and we vary P_o.

where $\Delta\hat{H}_o$ is the volumetric enthalpy at the point at which $v_e = 0$ (reservoir enthalpy), and the hat indicates values per unit volume. Here, the volumetric enthalpy change of a perfect gas caused by the decompression from P_g to P_o is given by [36].

$$\Delta\hat{H} = \frac{\gamma P_g}{\gamma - 1}\left[1 - \left(\frac{P_o}{P_g}\right)^{(\gamma-1)/\gamma}\right]. \tag{A.2}$$

We have modified this model to explain the experimental results with liquid gas mixtures, assuming 1) the enthalpy change for the liquid phase is negligible and that the enthalpy change of the gas phase causes expansion of the bubbly fluid, 2) velocity equilibrium between gas and liquid. To obtain Eq. (A.1), the compressed gas should be released in a perfect vacuum. In our experiments, however, the inside of the low-pressure tank is not a perfect vacuum, and we need to account for the compression of the gas inside the low-pressure tank. Assuming the isentropic compression, the required energy $\Delta\hat{W}$ is computed by

$$\Delta\hat{W} = \int_{P_g}^{P_o} P_o \hat{V} \tag{A.3}$$

$$= P_o\left[\left(\frac{P_g}{P_o}\right)^{1/\gamma} - 1\right]. \tag{A.4}$$

These equations are for the gas phase. When the volume fraction of the gas phase is ϕ, the expansion velocity is calculated as

$$v_{\mathrm{H}} = \sqrt{2\phi(\Delta\hat{H} - \Delta\hat{W})/\rho_{\mathrm{f}}} \qquad (A.5)$$

$$= \left(\frac{2\phi}{\rho_{\mathrm{f}}} \frac{\gamma P_{\mathrm{g}} - P_{\mathrm{o}}}{\gamma - 1} \left[1 - \frac{\gamma P_{\mathrm{o}}}{\gamma P_{\mathrm{g}} - P_{\mathrm{o}}} \right.\right.$$
$$\left.\left. \times \left\{\left(2 - \frac{1}{\gamma}\right)\left(\frac{P_{\mathrm{g}}}{P_{\mathrm{o}}}\right)^{1/\gamma} - 1\right\}\right]\right)^{1/2}. \qquad (A.6)$$

We will refer to this model as "model H". Here we define a new parameter $\Delta\hat{H}_{\mathrm{mod}}$ as

$$\Delta\hat{H}_{\mathrm{mod}} = \phi(\Delta\hat{H} - \Delta\hat{W}). \qquad (A.7)$$

Alidibirov [7] has estimated the blast velocity with the assumption that the internal energy of gases inside the bubbles is transformed to kinetic energy. The change of the internal energy of compressed gas, $\Delta\hat{U}$, resulting from decompression can be written as

$$\Delta\hat{U} = \frac{P_{\mathrm{g}}}{\gamma - 1}\left[1 - \left(\frac{P_{\mathrm{o}}}{P_{\mathrm{g}}}\right)^{(\gamma-1)/\gamma}\right]. \qquad (A.8)$$

We have also modified this model, in the manner as Eqs. (A.3)–(A.5), to be applicable to our experiments:

$$v_{\mathrm{U}} = \sqrt{2\phi(\Delta\hat{U} - \Delta\hat{W})/\rho_{\mathrm{f}}} \qquad (A.9)$$

$$= \left(\frac{2\phi}{\rho_{\mathrm{f}}} \frac{\Delta P}{\gamma - 1}\left[1 - \gamma\frac{P_{\mathrm{o}}}{\Delta P}\left\{\left(\frac{P_{\mathrm{g}}}{P_{\mathrm{o}}}\right)^{1/\gamma} - 1\right\}\right]\right)^{1/2}. \qquad (A.10)$$

We will refer to this model as "model U".

Cagnoli et al. [37] explained the expansion velocity of powder–gas two-phase flow by assuming the isothermal expansion of mixture. This velocity is estimated as

$$v_{\mathrm{CT}} = -\sqrt{\frac{P_{\mathrm{g}}\phi}{\rho_{\mathrm{f}}}}ln\left(\frac{P_{\mathrm{o}}}{P_{\mathrm{g}}}\right). \qquad (A.11)$$

Eq. (A.11) is similar to the isothermal expansion of bubbly magma derived by Turcotte et al. [38]. We will refer to this model as "model CT".

The vesicularity dependence of the expansion velocity of these models is the same. However, the pressure dependence differs. Fig. A.1 shows that $v_{\mathrm{H}} \approx \sqrt{\gamma}v_{\mathrm{U}}$. This can be easily understood by considering the case when $P_{\mathrm{g}} \gg P_{\mathrm{o}}$ in Eqs. (A.6) and (A.10). In contrast, v_{CT} is quite different from v_{H} and v_{U} at large pressure differences. Assuming that there is constant temperature expansion, rather than adiabatic expansion, means that the gas receives some additional energy, $\Delta\hat{Q}$, from liquid phase to maintain a constant gas temperature. The contribution of $\Delta\hat{Q}$ increases as ΔP becomes larger. This difference becomes important when applied to a real volcanic eruption because the expected overpressure for the volcanic eruption is large. Thus, the true test of models should be done at large pressure differences.

We plot three of these calculated velocities with measured velocities in Fig. A.2 H1, U1, CT1. Fig. A.2 H1 shows the best agreement with measured velocities. The misfits are distributed around the predictions. There is no dependence of misfits on ΔP and ϕ (Fig. A.2 H2, H3). Fig. A.2 U1 explains the trends of the velocity, but most of measured velocities exceed the predictions. There is no dependence of misfits on ΔP and ϕ; however, most of misfits are distributed above the line $\Delta v = 0$. This result indicates that the expansion velocity is described by v_{H} and $v_{\mathrm{U}} \sim v_{\mathrm{H}}/\sqrt{\gamma}$. Fig. A.2 CT1 shows that this model cannot explain the experimental results when the expansion velocity is fast. In addition, Fig. A.2 CT2 shows that the misfits becomes larger when the pressure difference becomes larger. This represents the trend shown in Fig. A.1. We thus conclude that model H is appropriate to explain the expansion velocity of the bubbly fluid by a rapid decompression and that the heat exchange between liquid and gas phase is not rapid enough in our experiments to influence expansion.

Appendix B. Deformation of the bubble wall

Here we calculate the strain of the bubble wall. First, we consider an isolated bubble with inner R_1 and outer R_2 radii which has been relaxed at a pressure P_{g}, and the outside pressure suddenly changes to
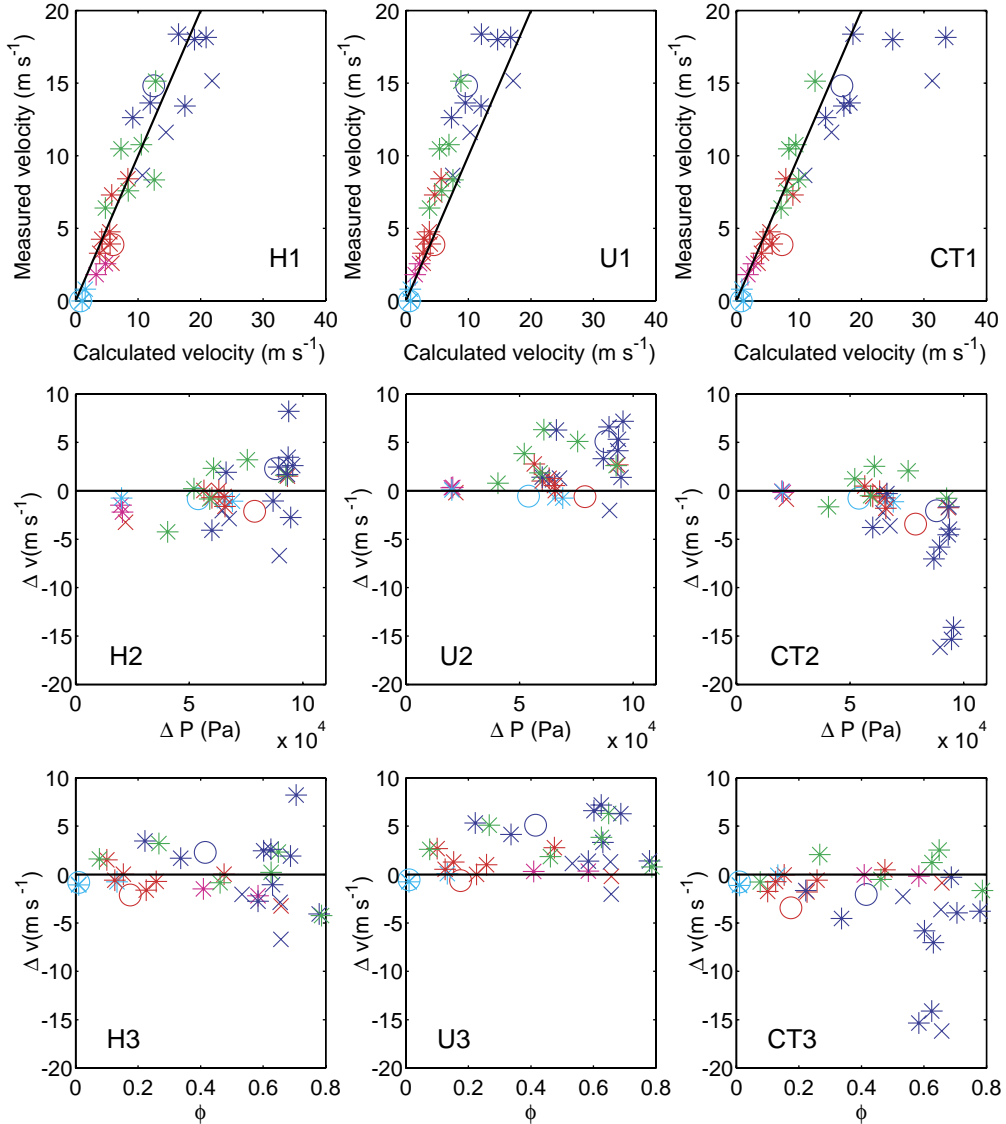
Fig. A.2. Comparison of three predictions for expansion velocities and experimental results. Symbols are the same as Fig. 6. (H1) Estimated expansion velocity for model H calculated by Eq. (A.6). (U1) Estimated expansion velocity for model U calculated by Eq. (A.10). (CT1) Estimated expansion velocity for model CT calculated by Eq. (A.11). (H2, U2, CT2) overpressure dependence of the misfits $\Delta v = v_{\text{measured}} - v_{\text{calculated}}$ for each model. (H3, U3, CT3) vesicularity dependence of the misfits for each model. Averaged misfits for H1, U1, and CT1 are 2.21, 2.83, and 3.18 m s^{-1}, respectively.

P_o. Using spherical polar coordinates with the origin at the center of the sphere (Fig. 8b), the displacement vector $\boldsymbol{u}$ is everywhere radial, and a function of r alone. Thus $\boldsymbol{curl}\ \boldsymbol{u} = 0$, and the equation of equilibrium becomes $\boldsymbol{grad}\ div \cdot \boldsymbol{u} = 0$ [39]. Radial displacement $u = ar + b/r^2$ can satisfy this equation. The radial

u_{rr} and tangential $u_{\theta\theta}$ components of the strain tensor are $u_{rr} = a - 2b/r^3$, $u_{\theta\theta} = a + b/r^3$, and radial stress σ^{rr} is calculated by

$$\sigma^{rr} = \frac{E}{(1+\sigma)(1-2\sigma)}\{(1-\sigma)u_{rr} + 2\sigma u_{\theta\theta}\}, \quad \text{(B.1)}$$

where σ is Poisson's ratio. Using the boundary conditions $\sigma^{rr}(r=R_1)=0$, $\sigma^{rr}(r=R_2)=-(P_o-P_g)$, $u_{\theta\theta}$ becomes

$$u_{\theta\theta} = \frac{-(P_o - P_g)R_2^3}{E(R_2^3 - R_1^3)}\left\{(1 - 2\sigma) + (1 + \sigma)\frac{R_1^3}{2r^3}\right\}.$$
(B.2)

Assuming the vesicularity ϕ is equal to $(R_1/R_2)^3$, $u_{\theta\theta}$ at R_1 is

$$u_{\theta\theta}(r = R_1) = \frac{-(P_o - P_g)}{E(1 - \phi)}\left\{(1 - 2\sigma) + \frac{1}{2}(1 + \sigma)\right\}.$$
(B.3)

References

[1] P.W. Lipman, D.R. Mullineaux (Eds.), The 1980 Eruptions of Mount St. Helens, Washington, USGS, Washington, D.C., 1981.

[2] M. Alidibirov, D.B. Dingwell, Magma fragmentation by rapid decompression, Nature 380 (1996) 146–148.

[3] R.S.J. Sparks, The dynamics of bubble formation and growth in magmas: a review and analysis, J. Volcanol. Geotherm. Res. 3 (1978) 1–37.

[4] H.M. Mader, Conduit flow and fragmentation, in: J.S. Gilber, R.S.J. Sparks (Eds.), The Physics of Explosive Volcanic Eruptions, vol. 145, Geological Society, London, 1998, pp. 51–71.

[5] K.V. Cashman, B. Sturtevant, P. Papale, O. Navon, Magmatic fragmentation, in: H. Sigurdsson, et al., (Eds.), Encyclopedia of Volcanoes, Academic Press, San Diego, 2000, pp. 421–430.

[6] A.R. McBirney, T. Murase, Factors governing the formation of pyroclastic rocks, Bull. Volcanol. 34 (1971) 373–384.

[7] M.A. Alidibirov, A model for viscous magma fragmentation during volcanic blasts, Bull. Volcanol. 56 (1994) 459–465.

[8] Y. Zhang, A criterion for the fragmentation of bubbly magma based on brittle failure theory, Nature 402 (1999) 648–650.

[9] S.L. Webb, D.B. Dingwell, Non-Newtonian rheology of igneous melts at high stresses and strain rates: experimental results for rhyolite, andesite, basalt, and nephelinite, J. Geophys. Res. 95 (1990) 15695–15701.

[10] P. Papale, Strain-induced magma fragmentation in explosive eruptions, Nature 397 (1999) 425–428.

[11] M. Ichihara, D. Rittel, B. Sturtevant, Fragmentation of a porous viscoelastic material: implications to magma fragmentation, J. Geophys. Res. 107 (2002), doi:10.1029/2001JB000591.

[12] H.M. Gonnermann, M. Manga, Explosive volcanism may not be an inevitable consequence of magma fragmentation, Nature 426 (2003) 432–435.

[13] A.A. Proussevitch, D.L. Sahagian, A.T. Anderson, Dynamics of diffusive bubble growth in magmas: isothermal case, J. Geophys. Res. 98 (1993) 22283–22307.

[14] I. Sugioka, M. Brusik, Explosive fragmentation of erupting magma, Nature 373 (1995) 689–692.

[15] A. Toramaru, Numerical study of nucleation and growth of bubbles in viscous magmas, J. Geophys. Res. 100 (1995) 1913–1931.

[16] H.M. Mader, J.C. Phillips, R.S.J. Sparks, Dynamics of explosive degassing of magma: observations of fragmenting two-phase flow, J. Geophys. Res. 101 (24) (1996) 5547–5560.

[17] C. Martel, D.B. Dingwell, O. Spieler, M. Pichavant, M. Wilke, Fragmentation of foamed silicic melts: an experimental study, Earth Planet. Sci. Lett. 178 (2000) 47–58.

[18] C. Martel, D.B. Dingwell, O. Spieler, M. Pichavant, M. Wilke, Experimental fragmentation of crystal- and vesicle-bearing silicic melts, Bull. Volcanol. 63 (2001) 398–405.

[19] C.C. Mourtada-Bonnefoi, H.M. Mader, Experimental observations of the effect of crystals and pre-existing bubbles on the dynamics and fragmentation of vesiculating flows, J. Volcanol. Geoth. Res. 129 (2004) 83–97.

[20] O. Spieler, B. Kennedy, U. Kueppers, D.B. Dingwell, B. Scheu, J. Taddeucci, The fragmentation threshold for pyroclastic rocks, Earth Planet. Sci. Lett. 226 (2004) 139–148.

[21] C.C. Mourtada-Bonnefoi, D. Laporte, Kinetics of bubble nucleation in a rhyolitic melt: an experimental study of the effect of ascent rate, Earth Planet. Sci. Lett. 218 (2004) 521–537.

[22] H.M. Mader, M. Manga, T. Koyaguchi, The role of laboratory experiments in volcanology, J. Volcanol. Geoth. Res. 129 (2004) 1–5.

[23] I.W. Hamley, Introduction to Soft Matter: Polymers, Colloids, Amphiphiles and Liquid Crystals, John Wiley & Sons, 2000.

[24] J.H. Fink, S.W. Kieffer, Estimate of pyroclastic flow velocities resulting from explosive decompression of lava domes, Nature 363 (1993) 612–615.

[25] L.G. Mastin, Thermodynamics of gas and steam-blast eruptions, Bull. Volcanol. 57 (1995) 85–98.

[26] A.A. Proussevitch, D.L. Sahagian, V.A. Kutolin, Stability of foams in silicate melts, J. Volcanol. Geotherm. Res. 59 (1993) 161–178.

[27] S.J. Lane, B.A. Chouet, J.C. Phillips, P. Dawson, G.A. Ryan, E. Hurst, Experimental observations of pressure oscillations and flow regimes in an analogue volcanic system, J. Geophys. Res. 106 (2001) 6461–6476.

[28] S. Hurwitz, O. Navon, Bubble nucleation in rhyolitic melts: experiments at high pressure, temperature, and water content, Earth Planet. Sci. Lett. 122 (1994) 267–280.

[29] B. Voight, Time scale for the first moments of the May 18 eruption, in: P.W. Lipman, D.R. Mullineaux (Eds.), The 1980 Eruptions of Mount St. Helens, Washington, USGS, Washington, D.C., 1981, pp. 69–86.

[30] N.G. Lensky, O. Navon, V. Lyakhovsky, Bubble growth during decompression of magma: experimental and theoretical investigation, J. Volcanol. Geotherm. Res. 129 (2004) 7–22.

[31] G. Heiken, K. Wohletz, Volcanic Ash, University of California Press, Berkeley, 1985.

[32] C. Klug, K.V. Cashman, Permeability development in vesiculating magmas: implications for fragmentation, Bull. Volcanol. 58 (1996) 87–100.

[33] J.C. Eichelberger, C.R. Carrigan, H.R. Westrich, R.H. Price, Non-explosive silicic volcanism, Nature 323 (1986) 598–602.

[34] C. Jaupart, C.J. Allegre, Gas content, eruption rate and instabilities of eruption regime in silicic volcanoes, Earth Planet. Sci. Lett. 102 (1991) 413–429.

[35] A.W. Woods, T. Koyaguchi, Transitions between explosive and effusive eruptions of silicic magmas, Nature 370 (1994) 641–644.

[36] L.D. Landau, E.M. Lifshitz, Fluid Mechanics Course of Theoretical Physics, vol. 6, Butterworth-Heinemann, Oxford, 1959.

[37] B. Cagnoli, A. Barmin, O. Melnik, R.S.J. Sparks, Depressurization of fine powders in a shock tube and dynamics of fragmented magma in volcanic conduits, Earth Planet. Sci. Lett. 204 (2002) 101–113.

[38] D.L. Turcotte, H. Ockendon, J.R. Ockendon, S.J. Cowley, A mathematical model of vulcanian eruptions, Geophys. J. Int. 103 (1990) 211–217.

[39] L.D. Landau, E.M. Lifshitz, Theory of Elasticity Course of Theoretical Physics, vol. 7, Butterworth-Heinemann, Oxford, 1959.